Optics & Laser Technology 163 (2023) 109356

Contents lists available at ScienceDirect

Optics and Laser Technology

journal homepage: www.elsevier.com/locate/optlastec

Full length article

PAIM (πM): Portable AI-enhanced fluorescence microscope for real-time target detection

Ziao Jiao [a,b,1], Zhenya Zang [a,b,1], Quan Wang [a,b], Yu Chen [c], Dong Xiao [a,b], David Day Uei Li [a,b,*]

[a] Department of Biomedical Engineering, University of Strathclyde, Glasgow G1 1XQ, Scotland, UK
[b] Strathclyde Institute of Pharmacy and Biomedical Sciences, University of Strathclyde, Glasgow G4 0RE, Scotland, UK
[c] Department of Physics, University of Strathclyde, Glasgow G4 0RE, Scotland, UK

ARTICLE INFO

Keywords:
Imaging systems
Microscopy
Biological imaging
Neural networks
Systems design

ABSTRACT

We proposed a portable AI fluorescence microscope (πM) based on a webcam and the NVIDIA Jetson Nano (NJN), integrating edge computing techniques for real-time target detection. πM achieves a physical magnification of ×5 and can resolve 228.1 lp/mm USAF features. Prepared microscopic samples and fluorescent polystyrene (PS) beads can be imaged clearly. πM's body was fabricated by a 3D printer, weighing ~ 250 g with dimensions of 145 mm × 172 mm × 144 mm (L × W × H), costing ~$300. It has a similar brightfield imaging quality compared to benchtop microscopes (~$13,000). The customized convolution neural network (CNN) inside the NJN can realize feature extraction, real-time PS bead counting, and red blood cell counting without data transfer and offline image processing. Compared with two model-free image processing methods (OpenCV and CLIJ2), our CNN method is robust in bead counting at different concentrations. Six aggregated beads can be correctly counted with 80 % accuracy. Regarding feature extraction and human RBC counting, our CNN also obtained closer results to the ground truth (GT) than the CLIJ2 method (GT: 201; CNN: 196; CLIJ2: 189). With a miniature size and real-time analysis, πM has potential in point-of-care testing, field microorganism detection, and clinical diagnosis in resource-limited areas.

1. Introduction

Microscopes can unveil biological and biochemical processes. In the last two decades, 3D printing techniques, MEMS systems, and diffractive optical elements have miniaturized microscope systems. Besides, we can develop compact microscopes using smartphones thanks to new CMOS sensors and well-designed optical lenses. These miniature microscopes are user-friendly, portable, and low-cost compared to laboratory microscopes. They can facilitate the diagnosis of sickle cell disease [1,2], sperm cell monitoring [3,4], and the detection of hazardous materials in drinking water in resource-limited areas [5,6]. We can classify these miniature microscopes into open-source and smartphone-based.

Many researchers use 3D printers to fabricate compact and low-cost microscope systems. Bowmen et al. established the OpenFlexure microscope [7–9]. It has already been employed for educational, scientific, and clinical applications in Tanzania and Kenya. Delmans and Haseloff proposed the μCube framework for 3D printing optomechanical parts for users to reconfigure their microscopes [10] quickly. Diederich et al. [11] also developed similar work. They developed microscopic components as LEGO-like building blocks to establish more complex systems. The cheapest microscope, the Foldscope, was fabricated by origami, costing less than $1. It can realize brightfield and fluorescence imaging [12].

Furthermore, more scientific and precise experiments can be achieved in open-source portable microscopes, such as real-time in-vivo neuron imaging [13] and single-molecule detection [14]. Artificial neural networks (ANNs) have recently enhanced portable microscopes' data processing capacity. Shen et al. used only one aspherical lens to build a microscope. They used a deep learning algorithm to improve the resolution power and minimize optical aberrations [15]. Besides these intensity-based microscopes [16–18], Ozcan et al. used off-the-shelf devices and 3D printers to develop portable quantitative phase microscopes and holographic microscopes [19]. They used ANNs or iterative algorithms to recover samples' morphology instead of optical lenses [20–23]. Harvey et al. developed a low-cost 3D-printed Fourier ptychography microscope based on a Raspberry Pi. This system can computationally construct images with a high space-bandwidth product

* Corresponding author.
E-mail address: David.li@strath.ac.uk (D.D. Uei Li).
[1] These authors contribute equally.

https://doi.org/10.1016/j.optlastec.2023.109356
Received 8 October 2022; Received in revised form 9 February 2023; Accepted 7 March 2023
Available online 14 March 2023

(25-megapixel with sub-micron resolution). They also used a novel algorithm to minimize aberrations [24]. Cacace et al. published design guidelines for a compact off-axis holographic microscope. They successfully used their prototype image flowing marine microalgae, polystyrene beads, E.coli bacteria, and microplastics [25]. To solve the problem of malaria diagnosis in remote regions where benchtop microscopes are unavailable, Gordon et al. designed a portable microscope with monochromatic visible illumination with a long working distance singlet aspheric objective lens. The detection limit can reach 0.18 parasites per 100 red blood cells [26].

Smartphone-based microscopes are easier to operate than open-source microscopes. Ozcan et al. developed different smartphone-based microscopes for imaging viruses [27] and DNA molecules [28], detecting Giardia lamblia cysts [29], and screening sickle cells [30]. They combined a smartphone with optical fiber arrays to develop a high-resolution computational microscope. They used the Wiener deconvolution algorithm to reconstruct images of blood smear samples [31]. Trofymchuk et al. built a smartphone microscope and carried out a single-molecule detection assay for DNA specific to antibiotic-resistant Klebsiella pneumonia [32]. Lee and Yang developed a lensless smartphone-based microscope by removing the camera lens [33]. They made a compact system using ambient light illumination. This microscope can capture ultra-wide field-of-view (FOV) images with a sub-micron resolution. Dai et al. coupled different colored polymer droplet lenses on smartphones to realize brightfield and fluorescence microscopes without optical lenses and filters. It can observe cells and tissues, count cells, and evaluate plasmid transfection and superoxide production [34]. Sung et al. developed a multicolor fluorescence smartphone microscope [35]. They used total-internal-reflection (TIR) guided illumination inside the glass slide. This configuration can enhance images' signal-to-background ratios. Müller et al. optimized a peptide nucleic acid (PNA) based fluorescence in situ hybridization (FISH) assay and used a smartphone microscope for rapid identification of pathogenic bacteria [36]. Liu et al. demonstrated a portable smartphone microscope called MUSE, the first practical implementation of microscopy with ultraviolet surface excitation. This MUSE is a powerful tool for point-of-care diagnostics, health monitoring, and environmental studies [37]. McKay et al. used iPhone and an additional iPhone camera lens to resolve optical absorption gaps in nailfold capillaries. The system has a 4 μm resolution with 1 mm^2 FOV [38]. Moreover, computational microscopes, such as Fourier ptychography microscopes [39], phase contrast microscopes [40–43], and 3D phase microscopes [44,45], can also be constructed using smartphones.

Several deep-learning techniques have been developed to process images captured from portable microscopes [46–50]. Göröcs et al. developed a portable deep-learning imaging flow cytometer for drinking water analysis [51,52]. Zhang et al. constructed a magnetically modulated lensless cytometry for blood cell detection [53]. Wu et al. developed a lensless microscope for herpes simplex virus detection and used deep learning to reconstruct high-quality images [54]. O'Connor et al. developed a compact digital holographic microscope. The built-in long short-term memory (LSTM) neural networks successfully classified different animals' blood cells, normal and sickle blood cells from human blood [55]. The system can also screen blood cells for COVID-19 tests [56].

Here, we proposed a portable AI-enhanced fluorescence microscope with a real-time AI function. Most open-source microscopes have sophisticated optomechanical structures and require external devices such as laptops and computers. Smartphone microscopes are compact but have less computing power to process images. Instead, πM offers a balanced solution. Table. 1 lists the comparative analysis between πM and several similar existing schemes. Compared with these systems, our system shows innovation by combining the optical imaging parts and data processing unit with a straightforward mechanical structure and low cost. The reversed off-the-shelf webcam lens provides good imaging quality without sophisticated optimization algorithms and an optical design. Moreover, the neural network can be easily adjusted for different applications—the easy configuration and low-cost design are suitable for in-field network training and data collection.

πM costs ~$300 and weighs 670 g with a size of 145 mm × 172 mm × 144 mm. It has a × 5 physical magnification and can resolve 228.1 lp/mm using the USAF target as an object. πM has the following novelties: Firstly, it has an easy optical path and mechanical design. Anyone can design it without sufficient mechanical design experience; Secondly, πM allows real-time AI-enhanced analysis with NJN-embedded neural networks for specific applications, and data transfer to the cloud or servers is no longer needed.

We demonstrated πM by imaging samples and different fluorescent

Table 1
Comparative analysis between recent similar schemes.

	Optomechanical complexity	AI function	Resolution	Application	Dimensional size (L*W*H)	Cost
Bowman et al. [9]	High	No	0.48 μm	Brightfield, fluorescence, and polarization imaging	150*150*200 mm^3, ~500 g	~$250
Heintzman et al. [11]	High	No	0.6 μm	Observations of a transgenic Zebrafish expressing green fluorescent protein (GFP)	200*50*200 mm^3 (Alterable)	$140~$680 (Altertable)
Zhu et al. [15]	Low	Yes	0.66 μm	Brightfield imaging	200*200*400 mm^3	N/A
Zhou et al. [19]	Medium	No	1.15 μm	PRCs phase imaging, material metrology	370*320*80 mm^3	~ $5000
Ferraro et al. [25]	Low	No	0.58 μm	Holographic microscope, flowing marine microalgae, polystyrene beads, E.coli bacteria and microplastics imaging	~50*30*150 mm^3	~$880
Gordon et al. [26]	High	Yes	0.8 μm	Automated malarial parasitemia quantification in thin blood smears	300*200*130 mm^3	~$1318
Ozcan et al. [30]	Medium	Yes	< 1 μm	Sickle cell disease detection	Smartphone + 350 g	$60 + Smartphone
Trofymchuk et al. [32]	Medium	No	1.2 μm	DNA origami single molecule detection	~ 200*150*200 mm^3	~$4600
Jenkins et al. [37]	Medium	No	3–4 μm	Ultraviolet Surface Excitation microscopy	138.3*67.1*7.1 mm^3 (iPhone 6 s size)	iPhone 6 s + $10
Durr et al. [38]	Low	No	< 4 μm (central FOV) < 6 μm (peripheral)	Quantification of optical absorption gaps in nailfold capillaries, neutropenia screening	143.6*70.9*7.7 mm^3 (iPhone X size)	N/A
Kuang et al. [43]	Medium	Yes	N/A	Virtual phase contrast imaging	120*100*170 mm^3 400 g	Smartphone + $1 ~ 10
Our work	Low	Yes	1.62 μm	Aggregated RBCs segmentation and counting	145*172*144 mm mm^3, 250 g	$300

PS beads, realizing real-time feature extraction and counting of beads and human RBCs. We compared the OpenCV, CLIJ2, and our customized CNN methods in bead and human RBC counting experiments. Our CNN can recognize six aggregated beads with 80 % accuracy (OpenCV: three aggregated beads with 26 % accuracy; CLIJ2: six aggregated beads with 64 % accuracy). It shows results closer to the ground truth (GT) than the CLIJ2 method (GT: 201; CNN: 196; CLIJ2: 189) in human RBC recognition and counting. These experimental results provide a proof-of-principle debut of πM.

2. Method

2.1. πM framework

Fig. 1(a) shows the πM framework. The NJN acts as the central process unit (CPU) to control the system, containing illumination LEDs and a CMOS camera. Users can train and implement ANNs inside the NJN for real-time analysis. We used a laptop to control πM, but it can be replaced with a touch screen. Ray-tracing simulations (OpticStudio 2017) and experiments determine πM's dimensional size and optical paths. We utilized CAD software (Solidworks 2020) and 3D-printed the main body parts.

2.2. Imaging system design

Fig. 1(b) shows πM's optical path. We can use a white LED for brightfield or replace the LED with a different wavelength for fluorescence imaging. We used a biconcave and a scattering aspherical condenser lens to achieve Galilean expander collimation, with the biconcave lens expanding and the condenser collimating the light. We can adjust the angle α (α = 60°) between the illumination and detection optical axes to enhance the image contrast of transparent biological samples. It can also prevent the excitation light from being directly collected by the inverse webcam lens when we use πM for fluorescence observation.

In the optical detection path, we disassembled a webcam lens from an off-the-shelf internet webcam (ELP, Shenzhen, China), reversed and used it as an objective lens. We designed a holder to combine it with the camera sensor and the optical filter. We then harnessed the refitted webcam with an inverse webcam lens to a z-direction translation stage to adjust the focal plane. The webcam lens is already well-optimized; therefore, this setup can magnify samples with negligible optical aberrations (especially for spherical aberration).

Before designing mechanical structures, we calculated the distances between optical elements (ID_R and WD_R in Fig. 1(d)). Since we only knew a few parameters of the webcam lens working in the webcam optical path (Fig. 1(c)), we first used these parameters in combination with the paraxial approximation to calculate approximate values in Fig. 1(c). Then we reversed the system and obtained the corresponding parameters in Fig. 1(d).

Because the sensor is a color sensor (Sony IMX-317), the sampling frequency should be three times as high as the spatial frequency. The magnification ($PMAG_R$) is:

$$PMAG_R = \text{ceiling}\left(\frac{3 \times Pixelsize}{L_{res}}\right), \tag{1}$$

where L_{res} is the theoretical resolution and the pixel pitch is 1.62 μm. We set the minimum resolution to 1 μm for πM to observe biological samples and $PMAG_R = 5$. The imaging system functions for the webcam optical path in Fig. 1c are:

$$F = \frac{horizontal\ \ pixel\ \ number \times \text{pixel}\ \ \text{pitch} \times WD}{FOV} \approx ID, \tag{2}$$

$$PMAG = \frac{1}{PMAG_R} = \frac{horizontal\ \ pixel\ \ number \times \text{pixel}\ \ \text{pitch}}{FOV} \tag{3}$$

where the sensor's horizontal pixel number and the pixel pitch are 3840 and 1.62 μm, respectively. $PMAG_R$ is 5, and F (back focal length) is 3.6 mm. As a result, W_D is approximately 18 mm, WD_R is 3.6 mm, and ID_R is 18 mm.

Edmund Optics provided the black-box simulation file of the webcam lens (f/2.5, 3.6 mm M12 Lens). We estimated $ID_R = 13 \sim 18$ mm in ray-tracing simulations. We plotted WD_R vs ID_R, $PMAG_R$ vs ID_R, and $PMAG_R$ vs ID_R curves in Fig. 2(c-d). WD_R and $PMAG_R$ were tested at each data point five times to obtain mean values and standard variations (the error bars). We chose 14 mm as ID_R to achieve the average WD_R of 5.41 mm and an average lateral magnification of × 5.14.

2.3. Illumination path

We used simulated and experimental results to optimize πM's illumination path to obtain even illumination at the object plane, as shown in Fig. 3(a). To collimate lights at a shorter distance, we utilized a concave lens (LD2747, Thorlabs) and an aspherical lens (ACL2520U-DG15, Thorlabs) to constitute a Galilean collimator. *D1* and *D3* were set as 10 mm and 50 mm, respectively. We used the Zemax RAID operand to calculate *D2* = 8.037 mm. Fig. 3(b) shows experimental results before and after collimation. Corresponding line profiles are shown in Fig. 3(c). To better understand how collimated illumination affects the spatial

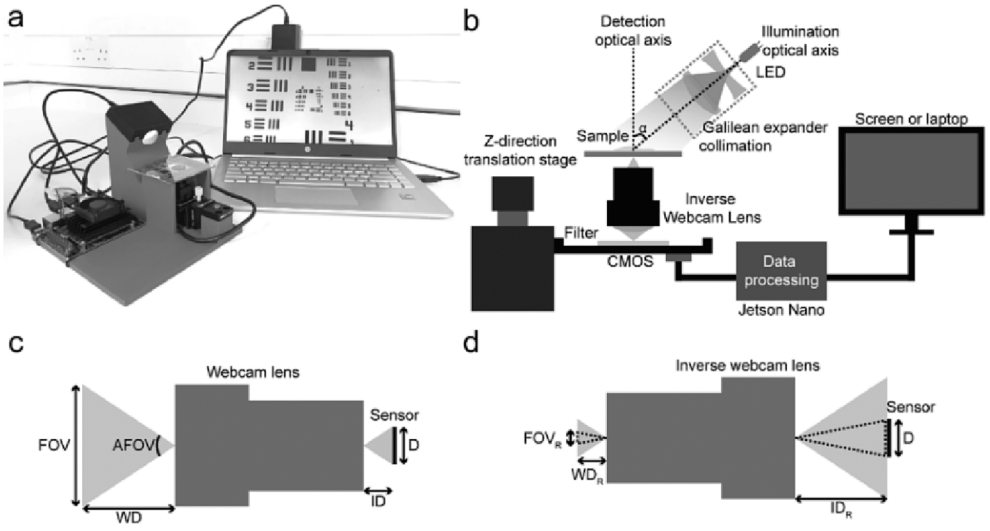

Fig. 1. (a)πM diagram. (b) πM optical path. A filter is inserted between the CMOS and the inverse webcam lens for observing fluorescent signals. The customized ANN in the NJN can realize real-time image analyses. (c) The original webcam optical path. (d) πM's optical path. Dashed triangle lines indicate the effective FOV in both object and image spaces (FOV: field of view, WD: working distance, ID: image distance, D: sensor's horizontal size, FOVR: πM's effective field of view, WDR: πM's working distance, IDR: πM's image distance).

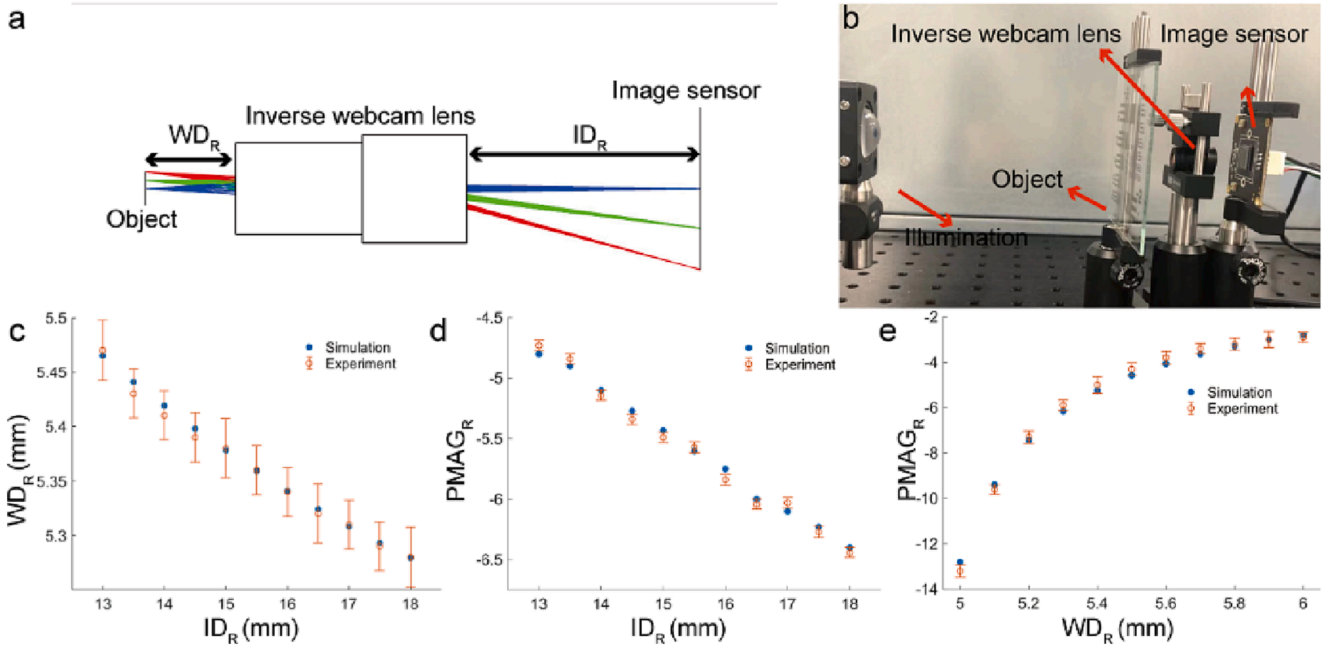

Fig. 2. Inverse webcam lens measurements. (a) Ray-tracing simulations of the inverse webcam lens. Blue, green, and red rays correspond to 0 mm, 0.5 mm, and 1 mm object height. (b) The experiment configuration. The object (R3L3S1P, Thorlabs) is illuminated by the white LED (LEDW7E, Thorlabs). Illumination lights are collimated by a diffusive surface aspherical lens (ACL2520U-DG15, Thorlabs). (c), (d) and (e) are relationships between ID_R, WD_R, and lateral magnifications. (For interpretation of the references to color in this figure legend, the reader is referred to the web version of this article.)

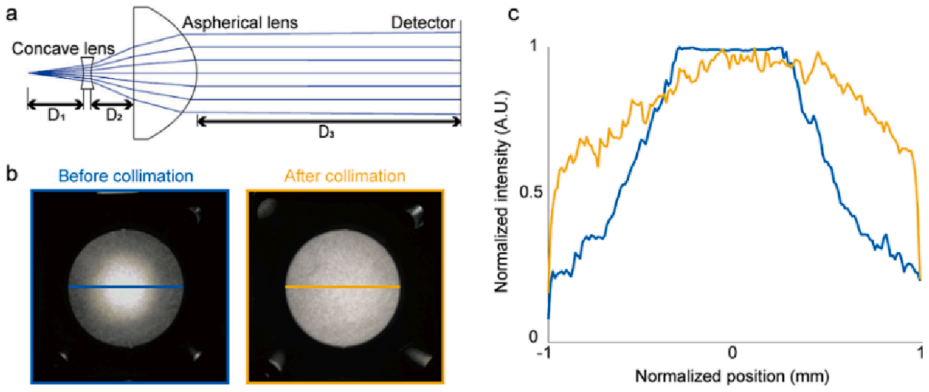

Fig. 3. Collimation light path. (a) The simulated collimation optical path. (b) Intensity distribution before and after collimation. (c) Corresponding line profiles of (b).

resolution of brightfield and fluorescence microscopes, we compared the PAI-M illumination with the critical and the Köhler illumination. We used the USAF-1951 (R3L3S1P, Thorlabs) as the test target and chose the white LED (LEDW7E, Thorlabs) illumination source for brightfield imaging. We used three different PS beads as samples (blue-green, Ex 430/Em 465; yellow-green, Ex 505/Em 515; red, Ex 580/Em 605; Thermofisher) for fluorescence imaging and chose appropriate single wavelength LED sources (430 nm, 505 nm, Lumex; LED591E, Thorlabs) for illumination. Sample preparation can be found in the section Method.

Fig. 4(a) illustrates three different illumination types. The light source is projected to the sample plane in critical illumination by a single convex lens (LD2746, Thorlabs). Although this configuration is the simplest way, the light filament will be imaged to the sample plane and affect image quality. Moreover, it can only illuminate a small region. However, the Köhler and PAI-M illumination can collimate light and provide even illumination at the sample plane covering larger areas. In our experiments, we constructed the Köhler illumination by a collector lens (LD2746, Thorlabs), a condenser lens (ACL2520U-DG15, Thorlabs), and two diaphragms (ID25, Thorlabs). πM's detailed illumination path is described in Method. Fig. 4(b) shows brightfield captured images with different illumination types. The corresponding line profiles of the 6th element of Group 7 (depicted in Fig. 4(b)) are shown in Fig. 4(c). We used Eq. (4) to judge the image quality:

$$C(\%) = \frac{I_{max} - I_{min}}{I_{max} + I_{min}} \tag{4}$$

where I_{max} and I_{min} are maximum and minimum pixel intensities, and a higher C means better image quality.

We also tested how the illumination field affects fluorescence images. Fig. 4(d) shows images of three different PS beads under different illumination types. The corresponding line profiles are shown in Fig. 4 (e). The emission wavelength determines the resolution of fluorescent signals. The optical filter can block the excitation light. The differences between these fluorescent bead images (under different illumination types) are insignificant. However, in brightfield imaging, the imaging

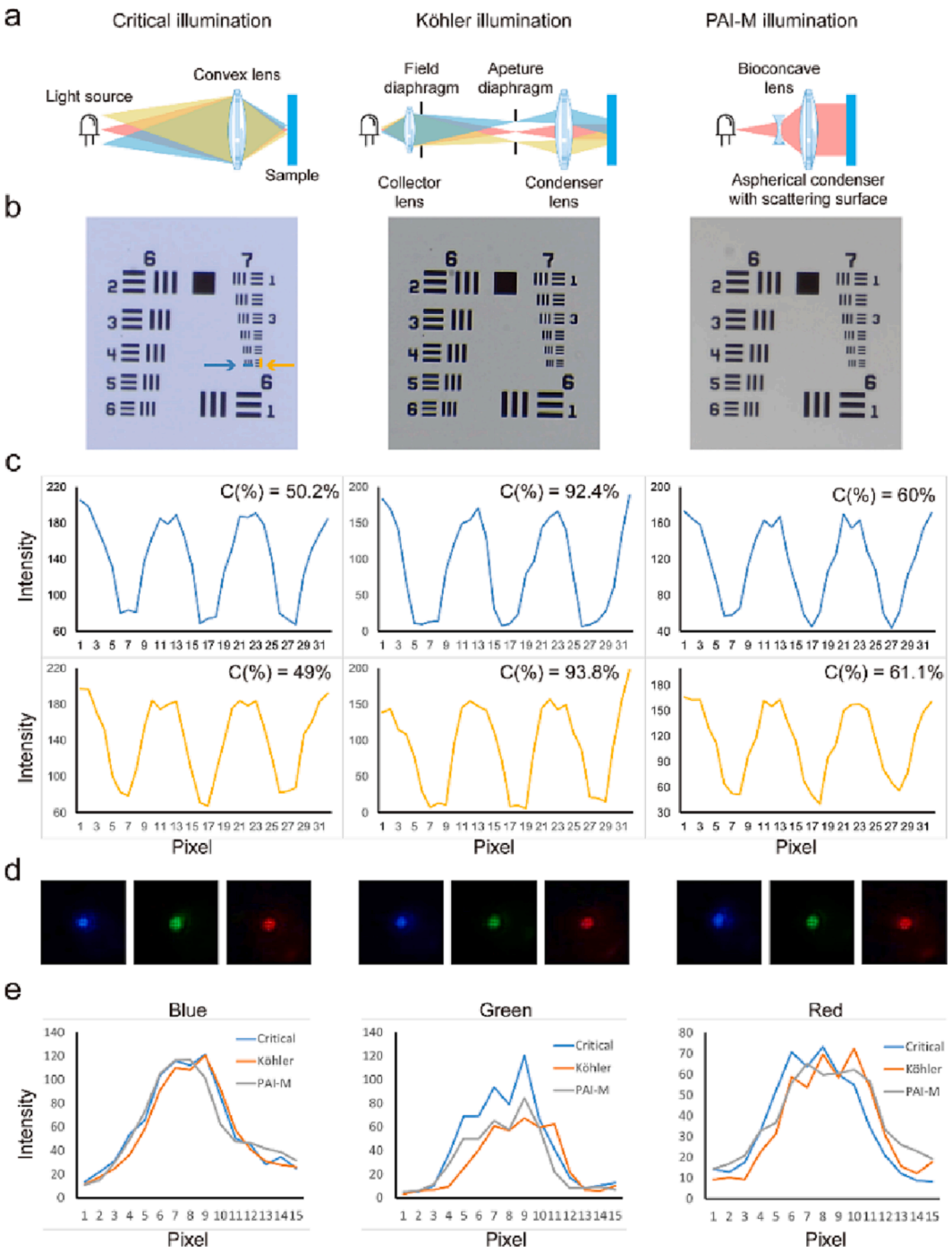

Fig. 4. Brightfield and fluorescence images are captured under different illumination setups. From (a)-(d), each column is related to the following illumination setup in Fig. 4(a). (a) Illustration of three different illumination setups. (b) Corresponding brightfield images were captured under different illumination types. (c) Horizontal and vertical line profiles of the 6th element of Group 7 in Fig. 4(b). (d) Blue, green, and red fluorescence images of PS beads. Corresponding line profiles are shown in Fig. 4(e). (For interpretation of the references to color in this figure legend, the reader is referred to the web version of this article.)

formation is due to the illumination light modulated by the object. According to the Abbe theory of microscope image formation, the image quality relies on the illumination light.

2.4. Body structures construction

We used Solidworks and a 3D printer to develop our πM (as shown in Fig. 5 with a twenty-cent coin as the dimensional reference). The detail to determine element sizes is described elsewhere (Method 2.2). The total size is 172 mm × 175 mm × 144 mm (L × W × H). We achieved Galilean expander collimation with a biconcave lens and a scattering aspherical condenser lens to collimate light (Fig. 5(b)). A redesigned webcam lens holder replaces the original to realize πM's optical path (Fig. 5(c)).

Fig. 6 shows CAD models of πM's parts. There are four components: the main body (Fig. 6(a)), the illumination cover (Fig. 6(b)), the webcam lens holder (Fig. 6(c)), and the sensor holder (Fig. 6(d)). The main body accommodates an NVIDIA Jetson Nano and contains an LED socket (LEDMT1F, Thorlabs), a concave lens (LD2746, Thorlabs), an aspherical convex lens (ACL2520U-DG15, Thorlabs), and an illumination cover

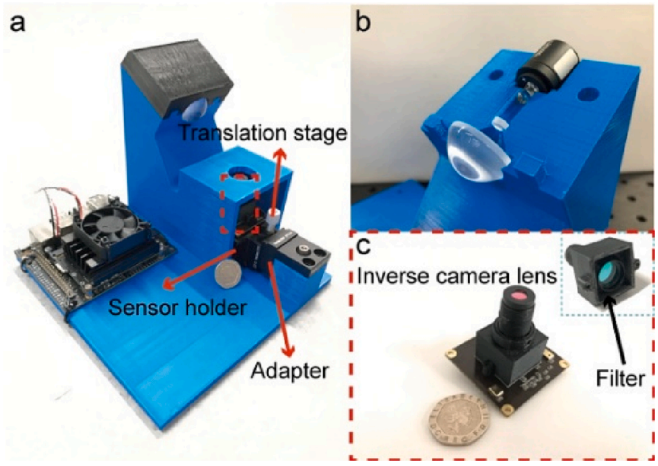

Fig. 5. Models of πM parts. (a) πM's schematic. (b) Illumination part. (c) The redesigned inverse webcam (Zoomed-in part in (a)). The vignette shows the back side of the webcam lens holder.

stabilizing components. We disassembled the webcam lens from the webcam and mounted it into the corresponding position (Inverse webcam lens) indicated in Fig. 6(c). The grey opaque parts in Fig. 6(c) are screw holes for coupling the webcam lens holder into the CMOS webcam. The sensor holder equipped with the redesigned microscopic webcam can be mounted to the Z-direction translation stage (DT12, Thorlabs) for adjusting the focus (Fig. 6(d)). Finally, we installed refitted webcam with a Z-direction translation stage to πM's main body through an adapter (DT12A, Thorlabs).

2.5. Foreground features extraction and the counting function

We implemented the proposed CNN-enhanced foreground feature extraction and counting functions based on a cascade neural network composed of a U-Net [57] and a VGG [58] network. To acquire results efficiently, we combined two networks to simultaneously realize segmentation and counting functions. The first output segmentation maps of the U-net network can seamlessly link to the VGG network for target counting. The U-net contains six down- and up-sampling layers, eventually producing precisely segmented images. We utilized the training data Broad Bioimage Benchmark Collection (BBBC 005) [59], including the pervasive cellular morphology captured by a fluorescence microscope. Despite unfocused cells, the U-Net can segregate foreground and background. This segregated image offers a solid pre-requisite for the counting task. The VGG network has seven convolutional and one fully connected (FC) layer. After two convolutions, the intensity and segregated images are fused to extract more spatial features. The FC layer then generates a scaler output indicating the number of cells. In experiments, the sensor's frame rate was from 30fps to 250fps (4 ms to 33 ms processing time). The average processing time on the Jetson Nano for each RGB 256*256 image is about 35fps (28.6 ms).

Although many image-processing algorithms exist for counting aggregated beads or cells, CNN is more accessible to combine with different neural networks. The layer's structures and corresponding input and output features can be easily customized. Moreover, transfer learning and amounts of open-source pre-trained neural networks can save time. Furthermore, the Jetson Nano, as a GPU acceleration calculation unit, is ideal for parallel matrix manipulations. Compared with other iterative algorithms, CNN can perform much better on the Jetson Nano.

In addition, compared with iterative algorithms, CNN can easily acquire many feature maps of aggregated and high-quantity targets. We compared the proposed method with the OpenCV and CLIJ2 [60] (an open-source unsupervised method) methods (Section 3.3, Section 3.4). Detailed information about the neural network can be found in the supplementary document.

2.6. Sample preparation

We used distilled water (ThermoFisher, USA) to prepare PS bead solutions with five concentrations (0.225×10^6, 0.45×10^6, 0.9×10^6, 1.8×10^6, and 3.6×10^6 beads/mL). The diameter of all PS beads is 10 μm. For fluorescent imaging, we used three different PS beads (blue-green, Ex 430/Em 465; yellow-green, Ex 505/Em 515; red, Ex 580/Em 605; Thermofisher) solutions with 1.8×10^6 beads/mL concentration. We used PS beads (505/515, Thermofisher) at different concentrations to test πM's real-time image foreground feature extraction and bead

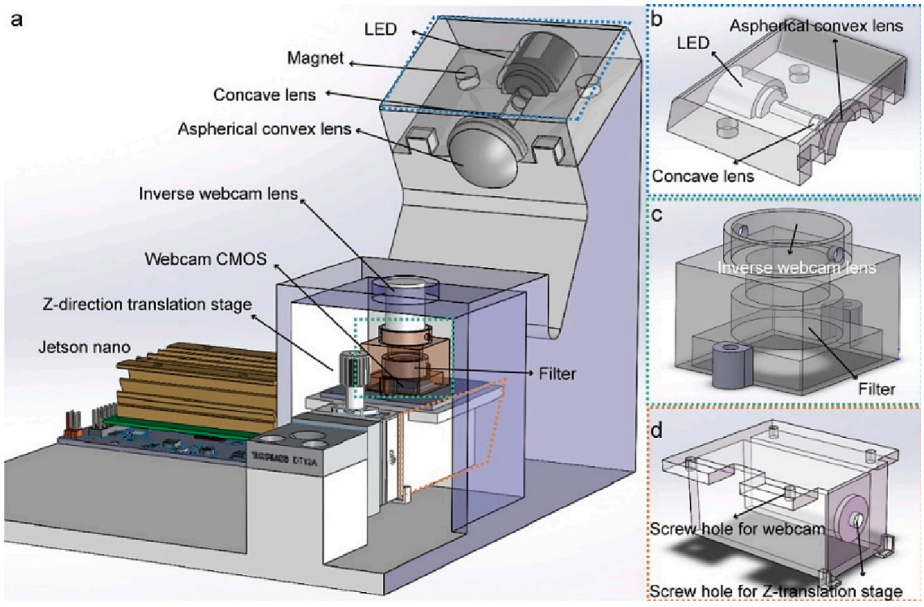

Fig. 6. Models of πM parts. (a) The main body for assembling all components. Four screw holes under NJN hold NJN to the main body. (a) πM's schematic. (b) The illumination cover is used for fixing LED and optical lenses. (c) Webcam lens holder for carrying the inverse webcam lens and an optical filter. (d) Sensor holder for holding the inverse webcam.

counting performances. We prepared each sample on the glass side (Corning, USA) with a 10 μL volume.

3. Results

3.1. Brightfield imaging

To test πM's brightfield imaging capacity, we used πM and a benchtop microscope (Olympus BX51, JP) to capture prepared dog skeletal muscle, Hydrilla leaf, and rabbit spinal cord microscope slides (AmScope, UK) under brightfield illumination. Using a benchtop microscope to observe samples, we chose a × 5 objective lens and the same sensor (IMX317-Sony). Notably, this compared experiment is limited to a comparison at x5 magnification because πM's magnification is also x5. Therefore, the magnification of the benchtop microscope candidates in comparison with our πM is limited to x5. Fig. 7 shows images of prepared microscope slides. The color temperature of different illumination sources causes the color difference in the background. Beyond that, during experiments, we found that images captured by a benchtop microscope were easier to be affected by artifacts that existed outside the focused sample plane (scratches and dust on glass, etc.). Through arrows in Fig. 7, we can see that these pictures' backgrounds captured by the benchtop microscope have more artifacts than those captured by πM, which means that under x5 magnification, the benchtop microscope's objective lens has a more considerable depth of field than πM's off-the-shelf objective lens. Pictures captured by a benchtop microscope have more artifacts, and these artifacts are at different layers of sample slides but simultaneously imaged to the sensor by the objective lens. We also used the USAF-1951 resolution target to validate πM's resolution. The target was illuminated by six LEDs (LED405E, LED465E, LED528HP, LED591E, LED630E, LEDW7E, Thorlabs). 228 line pair/mm targets (Element 6 of group 7) can be resolved under different wavelengths (Fig. 8, indicated by arrows).

3.2. Fluorescence imaging

We chose a blue LED (430 nm, Lumex) to excite blue-green beads, a yellow LED (505 nm, Lumex) to excite yellow-green beads, and an orange single wavelength LED (LED591E, Thorlabs) to excite red beads (see Section 2.5 Sample preparation). The corresponding optical filters (473/10, 520/10, 610/10, Edmund Optics) were chosen for observing fluorescent signals. Fig. 9 shows the bright field, fluorescence, and merged images of different PS beads. It also shows zoomed-in images encircled by yellow-dashed rectangles. The aggregated beads pointed by yellow arrows can be recognized in zoomed-in images. The samples' brightfield and fluorescence pictures can be captured under the same FOV by changing the webcam lens holder (Fig. 5c) and the optical filter.

3.3. Foreground feature extraction and bead counting

We used PS beads samples to show πM's real-time foreground feature extraction and counting performances. Table 2. shows the quantitative counting results of the images captured in the center FOV (800 μm2). Our CNN counting method is more robust than OpenCV because it can recognize aggregated beads. At lower (low and medium) concentrations, the CLIJ2 method shows a better performance. However, our CNN is more robust than the CLIJ2 method at higher concentrations. Our CNN can recognize aggregated targets. Fig. 10 shows foreground feature extraction and counting results at different concentrations. Fig. 10(a) shows local FOV sample images (low: 0.225 × 106 beads/mL, medium: 0.9 × 106 beads/mL, high: 3.6 × 106 beads/mL). The corresponding foreground feature extraction results are shown in the following rows. The *cv2.morphologyEx* function processes OpenCV input masks to eliminate the donut shape (shown in the CNN input mask). This configuration can enhance the counting accuracy of OpenCV. After segmentation, OpenCV and CNN masks were used as inputs for bead counting.

Furthermore, we used PS bead samples with different aggregated numbers to validate OpenCV, the CNN, and the CLIJ2 method in counting aggregate beads (from one to eight). We tested 50 other groups for each aggregated number. Fig. 10(b) shows the hot maps of counting accuracy for OpenCV (26 % accuracy for three aggregated beads), CNN (80 % accuracy for six aggregated beads), and CLIJ2(64 % accuracy for six aggregated beads). These results show that our CNN is better for aggregated target counting and segmentation. We also utilized the intersection of union (IoU) to evaluate the foreground extraction performance. We randomly selected 100 images from our test dataset and evaluated predicted masks. The average IoUs obtained from OpenCV, CNN, and CLIJ2 are 0.35, 0.8, and 0.79, respectively. It shows that our CNN method performs well in foreground feature extraction, like the CLIJ2 method (Fig. S2).

3.4. Red blood cells (RBC) extraction and counting

Further, we evaluated πM's functionalities on actual biological

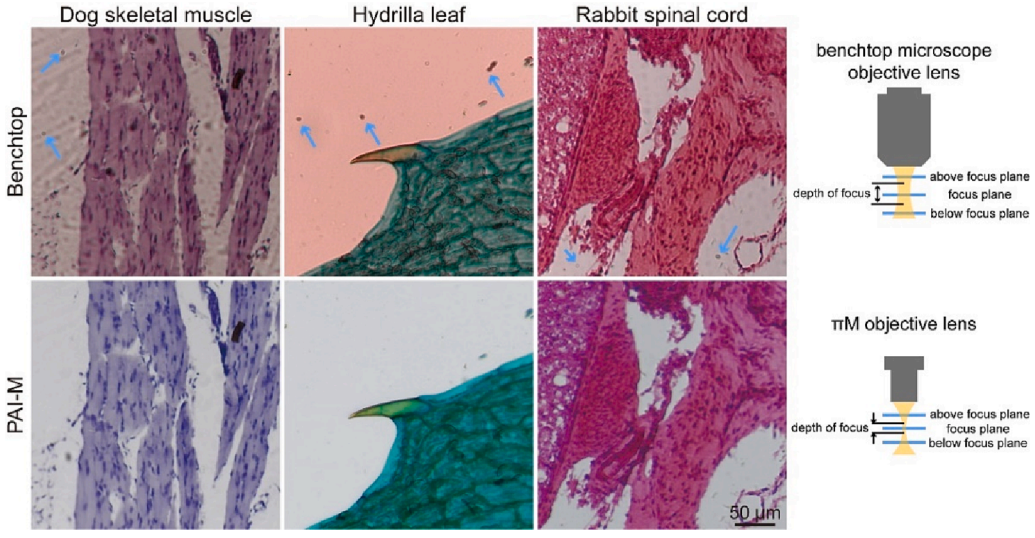

Fig. 7. Prepared microscope slides images captured by both PAI-M and benchtop brightfield microscope. We cropped these images for the same size and FOV for comparison, and the 50 μm scale bar is for all images. Blue arrows depict artifacts captured by benchtop microscope with x5 magnification. These artifacts are above or below the sample focus plane, and the right diagrams provide a detailed explanation. The benchtop microscope objective lens has a more extended depth of focus, so the sensor will collect information in this range simultaneously. However, the πM's objective lens has a smaller depth of focus range; this characteristic makes πM can only acquire information in a small range. Therefore, artifacts beyond the focus plane will be rejected. (For interpretation of the references to color in this figure legend, the reader is referred to the web version of this article.)

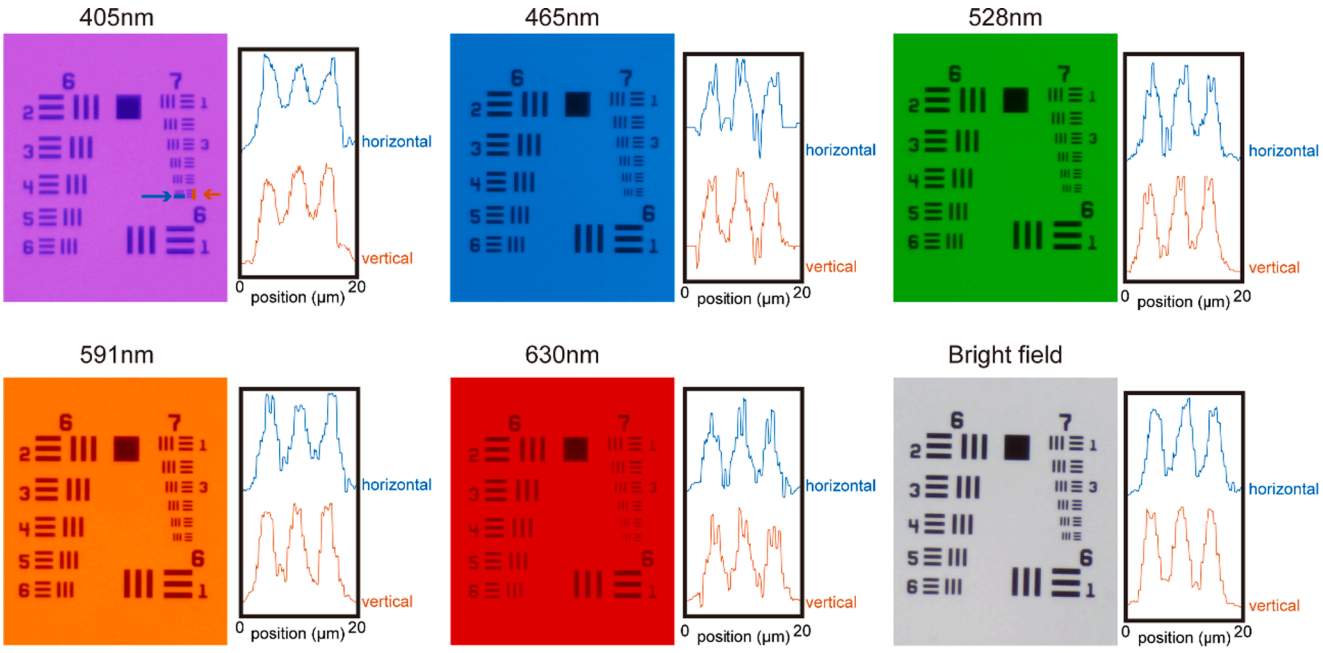

Fig. 8. πM's resolution under different illumination wavelengths. Each picture is cropped from the center FOV. Horizontal and vertical line profiles of the 6th element, Group 7 (indicated by arrows), are depicted beside each picture.

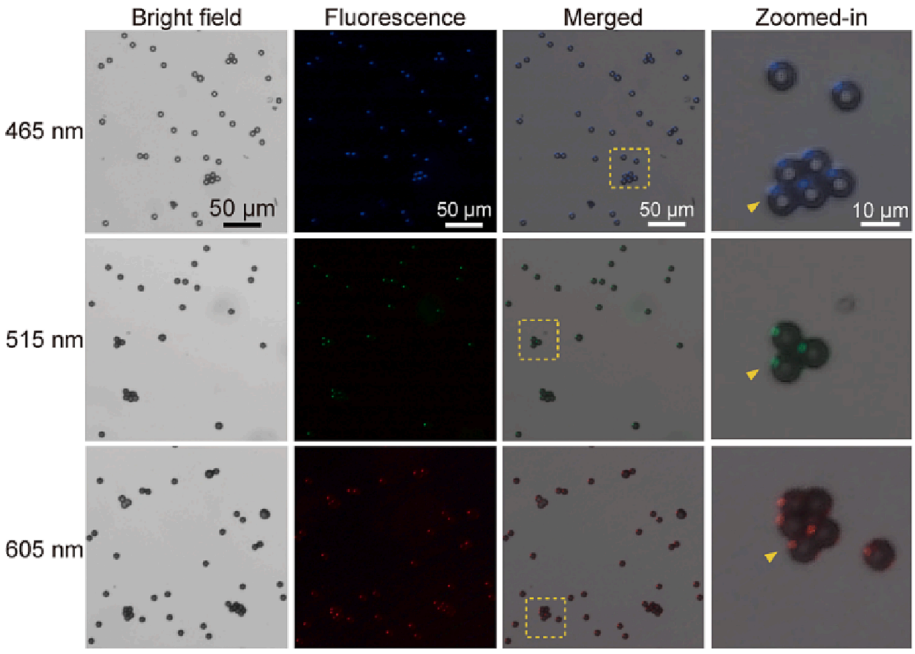

Fig. 9. Fluorescent PS beads image with different spectrums, and yellow arrows denote aggregated beads. The 50 μm scale bar is for the first three columns, and the 10 μm scale bar is for the last column. The fluorescent signals of PS beads in the Zoomed-in column are not located in the centre of the beads (yellow indicators), caused by the oblique illumination and the beads' 3D-rounded shapes. When the illumination light excited fluorescent beads obliquely, the light does not directly illuminate the beads' centres but their edges. Therefore, fluorescent signals appear on the beads' peripherals. These fluorescent signals are all located in the upper left of the beads. (For interpretation of the references to color in this figure legend, the reader is referred to the web version of this article.)

Table 2
Bead counting results. At each concentration, results were obtained by five captured images with different center FOVs. GT is the ground truth, Avg is the average value, and Std is the standard deviation.

	225 beads/μl		450 beads/μl		900 beads/μl		1800 beads/μl		3600 beads/μl	
	Avg	Std	Avg	Std	Avg	Std	Avg	Std	Avg	Std
GT	57	15.7	104.6	13.5	153.8	9.7	298.2	6.9	558.8	5.7
OpenCV	49.4	12	77	9.1	103.2	6.6	217.8	5.9	293.4	5.9
CNN	57.6	16.6	108.8	15.6	158.8	8.1	304.8	4.8	571.6	5.8
CLIJ2	57	15.7	103.8	12.3	149.6	10	282.8	6.6	504	6.1

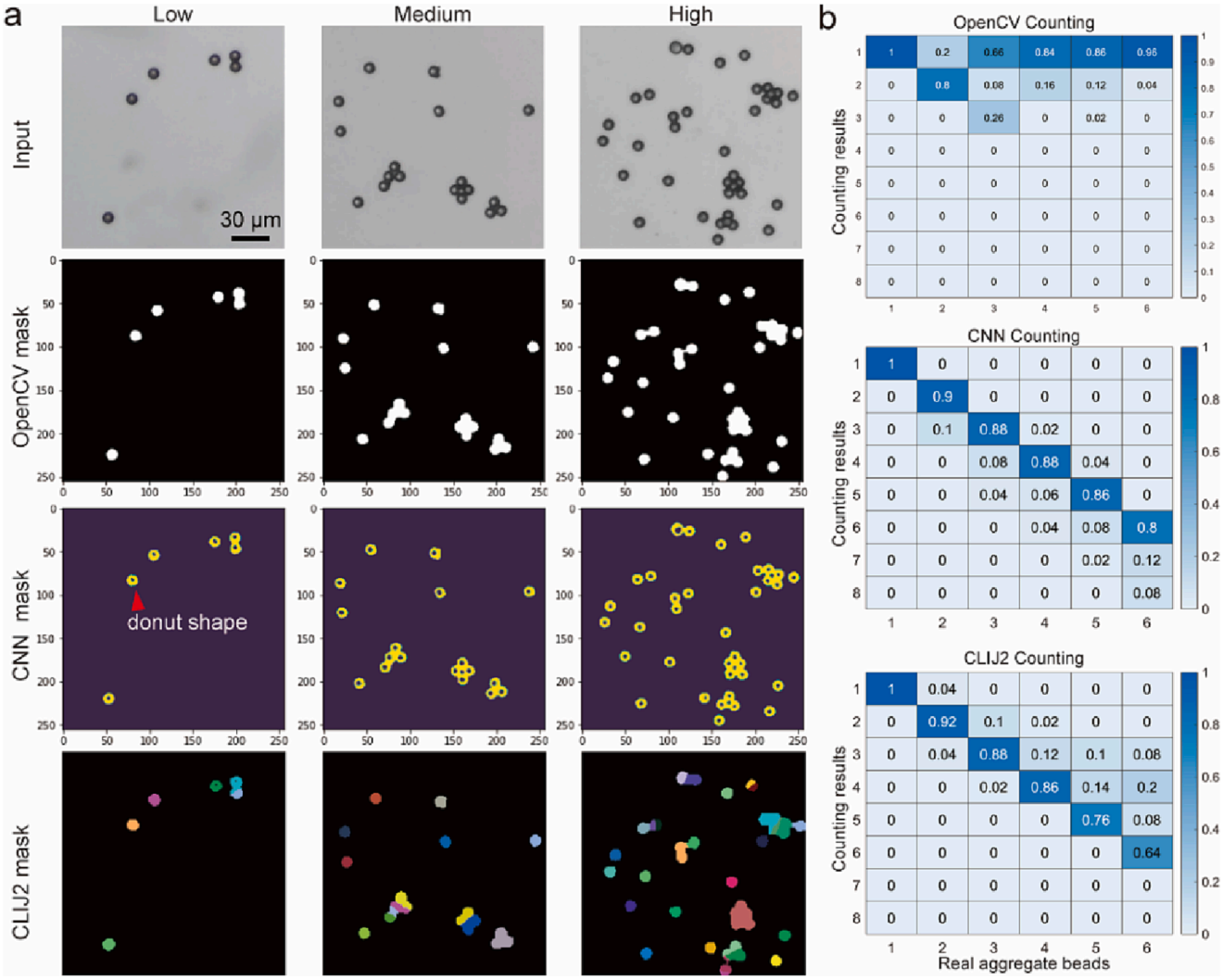

Fig. 10. πM's foreground feature extraction and quantitative counting results. (a) Sample images of local FOV and corresponding foreground feature extraction maps. Input: captured images. OpenCV, CNN, and CLIJ2 mask: Corresponding foreground feature extraction masks. (b) Accuracy hot maps of counting aggregated beads for our CNN, OpenCV, and CLIJ2 methods.

samples. We used prepared human RBCs smear samples as targets (Carolina, USA). According to previous bead experiments, the OpenCV method performs the worst. Therefore, we consider only our CNN and CLIJ2 here. We randomly selected 45 sub-regions from 10 samples for RBC extraction and counting. Table 3 shows statistical results, and the ground truth was examined using the benchtop microscope and a tally counter. Compared with CLIJ2, our CNN is more robust.

Fig. 11 shows original images of RBCs captured by πM and corresponding feature extraction maps using different methods. In the CNN mask row, RBCs are depicted by yellow labels, and these masks are used as the input for the counting neural network (Fig. S1). Each RBC is coded in the CLIJ2 mask row with a unique color, and adjacent RBCs do not share the same color. The extraction mask and counting results are obtained simultaneously. Although CLIJ2 is a model-free approach, prior knowledge about two parameters defining the distance of segregate cells and the precision of the segmentation boundary is needed. These two parameters should be fine-tuned to achieve optimal results. However, our data-driven CNN does not have this problem. We consistently obtained the same result for the same image in different trails.

Table 3
RBC counting results.

	Ground truth	CNN method	CLIJ2 method
Average counting results of 45 sub-regions	201	196	189
Counting standard deviation of 45 sub-regions	41	38	33

4. Discussion and prospect

Portable microscopes are low-cost, user-friendly, and compact. In resource-limited areas, they are powerful tools for biomedical research. πM's components can be easily reconfigured, and its optic-mechanical structure is simple. It contains a powerful AI-embedded system NJN and achieves image acquisition and real-time analysis without data transfer. Different from other portable microscopes, πM has several unique features. Users can: (1) easily customize their ANNs for specific applications, such as feature extraction, pattern recognition, and cell counting. (2) πM does not rely on network communication. The NJN, a robust calculation module, obtains real-time analysis. Users do not need to upload their captured images to servers and clouds. (3) πM can be an ANN training machine. Users can seamlessly capture images and customize and train their networks.

We used bead samples to validate πM's feature extraction and target counting functionalities. Experimental results show that our CNN is

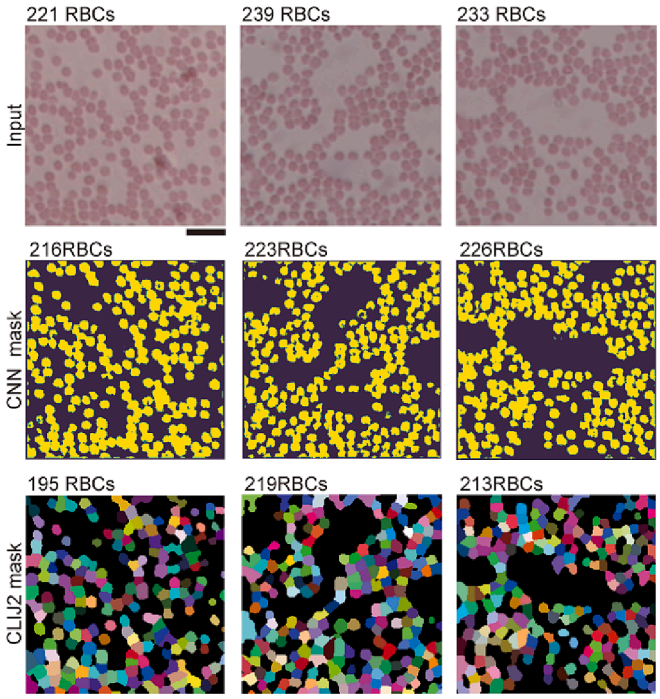

Fig. 11. Images of human red blood cells. The first row is the original pictures captured by πM, and the second and third rows are foreground feature extraction processed by our CNN and CLIJ2 methods. The number above each picture is the corresponding RBC counting result of the ground truth, CNN, and CLIJ2 methods. The scale bar under the top-left image is 20 μm. (For interpretation of the references to color in this figure legend, the reader is referred to the web version of this article.)

much more robust than OpenCV or CLIJ2 in bead counting. Six aggregated beads can be correctly counted with 80 % accuracy. Furthermore, we also used πM to image human red blood cell smear samples. We randomly selected different FOVs from RBC samples for recognition and counting. According to the statistical analysis, πM achieved closer results to the ground truth than CLIJ2. Both bead and RBC experiments show that πM has potential in biomedical image analysis, especially for those images and targets with sophisticated and dense features.

In this project, the initial aim is to develop a low-cost portable device for red blood cell imaging and counting. So, we put focus on this specific application. Meanwhile, considering the project funding, experiment condition, and ethical problem of biological experiments, more sophisticated biological experiments are not included in this study. Nevertheless, we chose several prepared teaching microscope slides as a comparison to show that our system has the potential to realize powerful biomedical imaging. In addition, although the segmentation and counting functions are realized only by brightfield images, fluorescent bead imaging implies that our system can be used for fluorescent imaging and diagnostics. Soon, we aim to upgrade πM to detect sickle cell diseases and hazardous microorganisms in drinking water in resource-limited regions at a relatively low cost. More fluorescent imaging and diagnostics will also be realized.

In the AI structure aspect, we cascaded the U-net network and the VGG network to get segmentation results with target counting numbers. This design diminishes the complexity of the system's data processing, and the robustness is also well maintained. However, our method is only validated for well-prepared samples, which means they do not have too many contaminants. In actual clinical applications, sophisticated contaminants distribution on sample slides can puzzle the AI algorithms to extract targets precisely. In future studies, we will try to find a proper way to overcome this problem without increasing the complexity of the network. We will artificially add some contaminants to test the robustness of our system.

5. Conclusion

We proposed a 3D-printed portable AI-supported fluorescence microscope (πM) for real-time target detection. Its size is 145 mm × 172 mm × 144 mm (L × W × H) and costs ~$300. We used a webcam by reversing the front lens to realize the imaging path. Using the USAF target as a test object, we used πM to resolve 228.1 lp/mm. πM can capture brightfield images similar to a benchtop microscope and can also clearly observe fluorescent PS beads (diameter = 10 μm). The embedded CNN can extract features in real-time and count beads accurately. Quantitative experiments show that our CNN can minimize counting imprecision caused by aggregated beads, and it is more robust than the OpenCV and the CLIJ2 method. The results of the red blood cell extraction and counting experiments prove that our πM has potential in real-time biomedical image analysis and disease detection.

Data availability

Data underlying the results presented in this paper are not publicly available but may be obtained from the authors upon request.

CRediT authorship contribution statement

Ziao Jiao: Investigation, Conceptualization, Validation. **Zhenya Zang:** Software. **Quan Wang:** Supervision. **Yu Chen:** . **Dong Xiao:** . **David Day Uei Li:** Supervision, Project administration.

Declaration of Competing Interest

The authors declare that they have no known competing financial interests or personal relationships that could have appeared to influence the work reported in this paper.

Data availability

Data will be made available on request.

Acknowledgements

The research has been supported by the Engineering and Physical Sciences Research Council under EPSRC Grant: EP/L01596X/1, the Royal Society of Edinburgh, and the China Scholarship Council.

Appendix A. Supplementary material

Supplementary data to this article can be found online at https://doi.org/10.1016/j.optlastec.2023.109356.

References

[1] S. Ilyas, M. Sher, E. Du, W. Asghar, Smartphone-based sickle cell disease detection and monitoring for point-of-care settings, Biosens. Bioelectron. 165 (2020), 112417.
[2] P.K. Das, S. Meher, R. Panda, A. Abraham, A Review of Automated Methods for the Detection of Sickle Cell Disease, IEEE Rev. Biomed. Eng. 13 (2020) 309–324.
[3] A. Amaral, J. Ramalho-Santos, Assessment of mitochondrial potential: implications for the correct monitoring of human sperm function, Int. J. Androl. 33 (1) (2010) e180–e186.
[4] S.M. Knowlton, M. Sadasivam, S. Tasoglu, Microfluidics for sperm research, Trends Biotechnol. 33 (4) (2015) 221–229.
[5] H. Nguyen, Y. Sung, K. O'Shaughnessy, X. Shan, W.C. Shih, Smartphone Nanocolorimetry for On-Demand Lead Detection and Quantitation in Drinking Water, Anal. Chem. 90 (19) (2018) 11517–11522.
[6] S.B. Tristan-Landin, A.M. Gonzalez-Suarez, R.J. Jimenez-Valdes, J.L. Garcia-Cordero, Facile assembly of an affordable miniature multicolor fluorescence microscope made of 3D-printed parts enables detection of single cells, PLoS One 14 (10) (2019) e0215114.

[7] J.P. Sharkey, D.C.W. Foo, A. Kabla, J.J. Baumberg, R.W. Bowman, A one-piece 3D printed flexure translation stage for open-source microscopy, Rev. Sci. Instrum. 87 (2) (2016), 025104.

[8] Q. Meng, K. Harrington, K. Harrington, J. Stirling, and R. Bowman, "The OpenFlexure Block Stage: sub-100 nm fibre alignment with a monolithic plastic flexure stage," *Optics Express*, Vol. 28, Issue 4, pp. 4763-4772 **28**(4), 4763–4772 (2020).

[9] B. Vodenicharski, C. Mkindi, D. Carbery, G. A. Mwakajinga, J. J. Baumberg, J. Knapper, J. T. Collins, J. Mduda, J. Stirling, L. White, P. T. Nyakyi, P. Cicuta, R. Bowman, S. McDermott, S. Dale, V. Mayagaya, V. L. Sanga, and Z. J. Lim, "Robotic microscopy for everyone: the OpenFlexure microscope," *Biomedical Optics Express*, Vol. 11, Issue 5, pp. 2447-2460 **11**(5), 2447–2460 (2020).

[10] M. Delmans, J. Haseloff, μCube: A Framework for 3D Printable Optomechanics, J. Open Hardware 2 (1) (2018).

[11] B. Diederich, R. Lachmann, S. Carlstedt, B. Marsikova, H. Wang, X. Uwurukundo, A. S. Mosig, and R. Heintzmann, "A versatile and customizable low-cost 3D-printed open standard for microscopic imaging," *Nature Commun.* 2020 11:1 **11**(1), 1–9 (2020).

[12] J.S. Cybulski, J. Clements, M. Prakash, Foldscope: Origami-Based Paper Microscope, PLoS One 9 (6) (2014) e98781.

[13] K. K. Ghosh, L. D. Burns, E. D. Cocker, A. Nimmerjahn, Y. Ziv, A. el Gamal, and M. J. Schnitzer, "Miniaturized integration of a fluorescence microscope," *Nature Methods* 2011 8:10 **8**(10), 871–878 (2011).

[14] J. W. P. Brown, A. Bauer, M. E. Polinkovsky, A. Bhumkar, D. J. B. Hunter, K. Gaus, E. Sierecki, and Y. Gambin, "Single-molecule detection on a portable 3D-printed microscope," *Nature Commun.* 2019 10:1 **10**(1), 1–7 (2019).

[15] H. Shen, J. Gao, Portable deep learning singlet microscope, J. Biophotonics 13 (6) (2020) e202000013.

[16] A.R. Miller, G.L. Davis, Z.M. Oden, M.R. Razavi, A. Fateh, M. Ghazanfari, F. Abdolrahimi, S. Poorazar, F. Sakhaie, R.J. Olsen, A.R. Bahrmand, M.C. Pierce, E. A. Graviss, R. Richards-Kortum, Portable, Battery-Operated, Low-Cost, Bright Field and Fluorescence Microscope, PLoS One 5 (8) (2010) e11890.

[17] Y.S. Zhang, J. Ribas, A. Nadhman, J. Aleman, Š. Selimović, S.C. Lesher-Perez, T. Wang, V. Manoharan, S.R. Shin, A. Damilano, N. Annabi, M.R. Dokmeci, S. Takayama, A. Khademhosseini, A cost-effective fluorescence mini-microscope for biomedical applications, Lab Chip 15 (18) (2015) 3661–3669.

[18] I. Nuñez, T. Matute, R. Herrera, J. Keymer, T. Marzullo, T. Rudge, F. Federici, Low cost and open source multi-fluorescence imaging system for teaching and research in biology and bioengineering, PLoS One 12 (11) (2017) e0187163.

[19] M. Niu, G. Luo, X. Shu, F. Qu, S. Zhou, Y.-P. Ho, Y.-P. Ho, N. Zhao, R. Zhou, and R. Zhou, "Portable quantitative phase microscope for material metrology and biological imaging," *Photonics Research*, Vol. 8, Issue 7, pp. 1253-1259 **8**(7), 1253–1259 (2020).

[20] A. Ozcan, M. Lee, and O. Yaglidere, "Field-portable reflection and transmission microscopy based on lensless holography," *Biomedical Optics Express*, Vol. 2, Issue 9, pp. 2721-2730 **2**(9), 2721–2730 (2011).

[21] A. Greenbaum, U. Sikora, A. Ozcan, Field-portable wide-field microscopy of dense samples using multi-height pixel super-resolution based lens-free imaging, Lab Chip 12 (7) (2012) 1242–1245.

[22] A. Greenbaum, N. Akbari, A. Feizi, W. Luo, A. Ozcan, Field-Portable Pixel Super-Resolution Colour Microscope, PLoS One 8 (9) (2013) e76475.

[23] A. C. Sobieranski, F. Inci, H. C. Tekin, M. Yuksekkaya, E. Comunello, D. Cobra, A. von Wangenheim, and U. Demirci, "Portable lensless wide-field microscopy imaging platform based on digital inline holography and multi-frame pixel super-resolution," *Light: Science & Applications* 2015 4:10 **4**(10), e346–e346 (2015).

[24] T. Aidukas, R. Eckert, A. R. Harvey, L. Waller, and P. C. Konda, "Low-cost, sub-micron resolution, wide-field computational microscopy using opensource hardware," *Scientific Reports* 2019 9:1 **9**(1), 1–12 (2019).

[25] T. Cacace, V. Bianco, B. Mandracchia, V. Pagliarulo, E. Oleandro, M. Paturzo, P. Ferraro, Compact off-axis holographic slide microscope: design guidelines, Biomed. Opt. Express 11 (2020) 2511–2532.

[26] P.D. Gordon, C. De Ville, J.C. Sacchettini, G.L. Coté, A portable brightfield and fluorescence microscope toward automated malarial parasitemia quantification in thin blood smears, *PLoS* ONE 17 (4) (2022) e0266441.

[27] Q. Wei, H. Qi, W. Luo, D. Tseng, S.J. Ki, Z. Wan, Z. Göröcs, L.A. Bentolila, T.T. Wu, R. Sun, A. Ozcan, Fluorescent imaging of single nanoparticles and viruses on a smart phone, ACS Nano 7 (10) (2013) 9147–9155.

[28] Q. Wei, W. Luo, S. Chiang, T. Kappel, C. Mejia, D. Tseng, R.Y.L. Chan, E. Yan, H. Qi, F. Shabbir, H. Ozkan, S. Feng, A. Ozcan, Imaging and sizing of single DNA molecules on a mobile phone, ACS Nano 8 (12) (2014) 12725–12733.

[29] H.C. Koydemir, Z. Gorocs, D. Tseng, B. Cortazar, S. Feng, R.Y.L. Chan, J. Burbano, E. McLeod, A. Ozcan, Rapid imaging, detection and quantification of Giardia lamblia cysts using mobile-phone based fluorescent microscopy and machine learning, Lab Chip 15 (5) (2015) 1284–1293.

[30] K. de Haan, H. Ceylan Koydemir, Y. Rivenson, D. Tseng, E. van Dyne, L. Bakic, D. Karinca, K. Liang, M. Ilango, E. Gumustekin, and A. Ozcan, "Automated screening of sickle cells using a smartphone-based microscope and deep learning," *npj Digital Medicine* 2020 3:1 **3**(1), 1–9 (2020).

[31] I. Navruz, A.F. Coskun, J. Wong, S. Mohammad, D. Tseng, R. Nagi, S. Phillips, A. Ozcan, Smartphone based computational microscopy using multi-frame contact imaging on a fiber-optic array, Lab Chip 13 (20) (2013) 4015–4023.

[32] K. Trofymchuk, V. Glembockyte, L. Grabenhorst, F. Steiner, C. Vietz, C. Close, M. Pfeiffer, L. Richter, M. L. Schütte, F. Selbach, R. Yaadav, J. Zähringer, Q. Wei, A. Ozcan, B. Lalkens, G. P. Acuna, and P. Tinnefeld, "Addressable nanoantennas with cleared hotspots for single-molecule detection on a portable smartphone microscope," *Nature Communications* 2021 12:1 **12**(1), 1–8 (2021).

[33] S.A. Lee, C. Yang, A smartphone-based chip-scale microscope using ambient illumination, Lab Chip 14 (16) (2014) 3056–3063.

[34] B. Dai, Z. Jiao, L. Zheng, H. Bachman, Y. Fu, X. Wan, Y. Zhang, Y. Huang, X. Han, C. Zhao, T. J. Huang, S. Zhuang, and D. Zhang, "Colour compound lenses for a portable fluorescence microscope," *Light: Science & Applications* 2019 8:1 **8**(1), 1–13 (2019).

[35] F. Campa, W.-C. Shih, and Y. Sung, "Open-source do-it-yourself multicolor fluorescence smartphone microscopy," *Biomedical Optics Express*, Vol. 8, Issue 11, pp. 5075-5086 **8**(11), 5075–5086 (2017).

[36] V. Müller, J.M. Sousa, H. Ceylan Koydemir, M. Veli, D. Tseng, L. Cerqueira, A. Ozcan, N.F. Azevedo, F. Westerlund, "Identification of pathogenic bacteria in complex samples using a smartphone based fluorescence microscope," *RSC*, Advances 8 (64) (2018) 36493–36502.

[37] Y. Liu, A.M. Rollins, R.M. Levenson, et al., Pocket MUSE: an affordable, versatile and high-performance fluorescence microscope using a smartphone, Commun Biol 4 (2021) 334.

[38] G.N. McKay, N. Mohan, I. Butterworth, A. Bourquard, Á. Sánchez-Ferro, C. Castro-González, N.J. Durr, Visualization of blood cell contrast in nailfold capillaries with high-speed reverse lens mobile phone microscopy, Biomed. Opt. Express 11 (2020) 2268–2276.

[39] S. Dong, K. Guo, P. Nanda, R. Shiradkar, G. Zheng, X. Heng, D. Erickson, L. R. Baugh, Z. Yaqoob, P. W. Sternberg, D. Psaltis, and C. Yang, "FPscope: a field-portable high-resolution microscope using a cellphone lens," *Biomedical Optics Express*, Vol. 5, Issue 10, pp. 3305-3310 **5**(10), 3305–3310 (2014).

[40] Z.F. Phillips, M.v. D'Ambrosio, L. Tian, J.J. Rulison, H.S. Patel, N. Sadras, A. v. Gande, N.A. Switz, D.A. Fletcher, L. Waller, Multi-Contrast Imaging and Digital Refocusing on a Mobile Microscope with a Domed LED Array, PLoS One 10 (5) (2015) e0124938.

[41] D. Jung, J. H. Choi, S. Kim, S. Ryu, W. Lee, J. S. Lee, and C. Joo, "Smartphone-based multi-contrast microscope using color-multiplexed illumination," *Scientific Reports* 2017 7:1 **7**(1), 1–10 (2017).

[42] B. Diederich, R. Wartmann, H. Schadwinkel, R. Heintzmann, Using machine-learning to optimize phase contrast in a low-cost cellphone microscope, PLoS One 13 (3) (2018) e0192937.

[43] Y. Bian, Y. Jiang, Y. Huang, X. Yang, W. Deng, H. Shen, R. Shen, C. Kuang, Smartphone phase contrast microscope with a singlet lens and deep learning, Opt. Laser Technol. 139 (2021), 106900.

[44] X. Meng, H. Huang, K. Yan, X. Tian, W. Yu, H. Cui, Y. Kong, L. Xue, C. Liu, S. Wang, Smartphone based hand-held quantitative phase microscope using the transport of intensity equation method, Lab Chip 17 (1) (2016) 104–109.

[45] B.K. Goud, D.D. Shinde, D.v. Udupa, C.M. Krishna, K.D. Rao, N.K. Sahoo, Low cost digital holographic microscope for 3-D cell imaging by integrating smartphone and DVD optical head, Opt. Lasers Eng. 114 (2019) 1–6.

[46] Y. Wu, Y. Luo, G. Chaudhari, Y. Rivenson, A. Calis, K. de Haan, and A. Ozcan, "Brightfield holography: cross-modality deep learning enables snapshot 3D imaging with brightfield contrast using a single hologram," *Light: Science & Applications* 2019 8:1 **8**(1), 1–7 (2019).

[47] T. Liu, K. de Haan, Y. Rivenson, Z. Wei, X. Zeng, Y. Zhang, and A. Ozcan, "Deep learning-based super-resolution in coherent imaging systems," *Scientific Reports* 2019 9:1 **9**(1), 1–13 (2019).

[48] Y. Rivenson, T. Liu, Z. Wei, Y. Zhang, K. de Haan, and A. Ozcan, "PhaseStain: the digital staining of label-free quantitative phase microscopy images using deep learning," *Light: Science & Applications* 2019 8:1 **8**(1), 1–11 (2019).

[49] Y. Rivenson, H. Ceylan Koydemir, H. Wang, Z. Wei, Z. Ren, H. Günaydln, Y. Zhang, Z. Göröcs, K. Liang, D. Tseng, A. Ozcan, Deep Learning Enhanced Mobile-Phone Microscopy, ACS Photonics 5 (6) (2018) 2354–2364.

[50] Y. Li, R. Zheng, Y. Wu, K. Chu, Q. Xu, M. Sun, Z.J. Smith, A low-cost, automated parasite diagnostic system via a portable, robotic microscope and deep learning, J. Biophotonics 12 (9) (2019) e201800410.

[51] Z. Göröcs, M. Tamamitsu, V. Bianco, P. Wolf, S. Roy, K. Shindo, K. Yanny, Y. Wu, H. C. Koydemir, Y. Rivenson, and A. Ozcan, "A deep learning-enabled portable imaging flow cytometer for cost-effective, high-throughput, and label-free analysis of natural water samples," *Light: Science & Applications* 2018 7:1 **7**(1), 1–12 (2018).

[52] Z. Göröcs, D. Baum, F. Song, K. de Haan, H. Ceylan Koydemir, Y. Qiu, Z. Cai, T. Skandakumar, S. Peterman, M. Tamamitsu, A. Ozcan, Label-free detection of Giardia lamblia cysts using a deep learning-enabled portable imaging flow cytometer, Lab Chip 20 (23) (2020) 4404–4412.

[53] Y. Zhang, M. Ouyang, A. Ray, T. Liu, J. Kong, B. Bai, D. Kim, A. Guziak, Y. Luo, A. Feizi, K. Tsai, Z. Duan, X. Liu, D. Kim, C. Cheung, S. Yalcin, H. Ceylan Koydemir, O. B. Garner, D. di Carlo, and A. Ozcan, "Computational cytometer based on magnetically modulated coherent imaging and deep learning," *Light: Science & Applications* 2019 8:1 **8**(1), 1–15 (2019).

[54] Y. Wu, A. Ray, Q. Wei, A. Feizi, X. Tong, E. Chen, Y. Luo, A. Ozcan, Deep Learning Enables High-Throughput Analysis of Particle-Aggregation-Based Biosensors Imaged Using Holography, ACS Photonics 6 (2) (2019) 294–301.

[55] A. Anand, B. Javidi, B. Andemariam, and T. O'Connor, "Deep learning-based cell identification and disease diagnosis using spatio-temporal cellular dynamics in compact digital holographic microscopy," *Biomedical Optics Express*, Vol. 11, Issue 8, pp. 4491-4508 **11**(8), 4491–4508 (2020).

[56] B. Javidi, B. T. Liang, J.-B. Shen, and T. O'Connor, "Digital holographic deep learning of red blood cells for field-portable, rapid COVID-19 screening," *Optics Letters*, Vol. 46, Issue 10, pp. 2344-2347 **46**(10), 2344–2347 (2021).

[57] O. Ronneberger, P. Fischer, T. Brox, U-Net: Convolutional Networks for Biomedical Image Segmentation, Lecture Notes in Comput. Sci. (including subseries Lecture Notes in Artificial Intelligence and Lecture Notes in Bioinformatics) 9351 (2015) 234–241.

[58] K. Simonyan and A. Zisserman, "Very Deep Convolutional Networks for Large-Scale Image Recognition," *3rd International Conference on Learning Representations, ICLR 2015* - Conference Track Proceedings (2014).
[59] V. Ljosa, K. L. Sokolnicki, and A. E. Carpenter, "Annotated high-throughput microscopy image sets for validation," *Nature Methods* 2012 9:7 **9**(7), 637–637 (2012).
[60] R. Haase, L.A. Royer, P. Steinbach, D. Schmidt, A. Dibrov, U. Schmidt, M. Weigert, N. Maghelli, P. Tomancak, F. Jug, E.W. Myers, CLIJ: GPU-accelerated image processing for everyone, Nat. Methods 17 (1) (2020) 5–6.